JOURNAL OF PROPULSION AND POWER
Vol. 8, No. 3, May–June 1992

Theoretical Modeling of the Interior Ballistic Processes in an Electrothermal Chemical Gun

J. L. Chen,* K. K. Kuo,† and F. B. Cheung‡
Pennsylvania State University, University Park, Pennsylvania 16802

A comprehensive theoretical model has been developed to describe the interior ballistic processes in an electrothermal chemical (ETC) gun. The model, which takes into account the plasma/working fluid interaction, predicts transient and spatial variations of the gun chamber pressure, instantaneous projectile motion, and gun muzzle velocity. A complete set of governing equations is derived from first principles of physics, and the governing system is solved by an implicit finite difference scheme. Two sets of pulse-forming network (PFN) discharge curves, with various peak power times and total discharge times, are employed to study the ETC gun performance. The numerical results show that a ballistic efficiency of more than 13% can be achieved for an exothermic working fluid (C_8H_{18}/H_2O_2). The breech pressure and projectile-base pressure exhibit double peaks during the ballistic cycle. The first peak is due to the initial discharge of a plasma jet into the gun chamber, whereas the second peak is the result of vigorous interactions between the plasma jet and the working fluid. The calculated maximum breech pressure is on the order of 400 MPa, and a typical muzzle velocity is on the order of 2 km/s. Comparison of present numerical results with limited available experimental data is made and found to be good.

Nomenclature

A_{cs} = area of projectile base
A_s = specific wetted area between droplet and gas phases
A_η, A_ζ = grid areas in η, ζ direction
a_P = acceleration of projectile
b = covolume
$C_{1,j}$, $C_{2,j}$ = coefficients in droplet number density equation
$C_{D,k}$ = drag force coefficient of kth droplet
C_f = sliding friction coefficient
C_{Pg} = specific heat of gas
$C_{\varepsilon 1}$, $C_{\varepsilon 2}$, C_μ = constants in k, ε equations
D_{eff} = effective diffusion coefficient
$D_{t,x}$, $D_{t,r}$ = total drag force in x, r directions
d_d, $d_{d,k}$ = droplet diameter, characteristic droplet diameter of kth group
d_e, d_w, d_s, d_n = coefficients of pressure-difference terms at east, west, south, and north sides of grid
d_m = maximum droplet size
d_t = hydraulic diameter of a tube
d_{32} = Sauter mean diameter
F'_D = engraving and sliding forces
F_R = resulting force normal to the band
f_I = friction factor of a rough pipe
f_s = friction factor of a smooth pipe
H = total energy = enthalpy + kinetic energy
ΔH_{fg} = heat of evaporation + sensible heat
$h_{\text{conv},d}$ = convection heat transfer coefficient at droplet surface
$h_{\text{rad},d}$ = radiation heat transfer coefficient at droplet surface
Δh_d = chemical energy released through droplet combustion
I_P = axial moment of inertia
K = coefficient due to density variation in pressure-correction equation
K_A = atomization rate constant
K_P = rotational constant
k = turbulent kinetic energy
L_c = length of Taylor cavity
n_j = number density of jth group droplet
$\dot{n}_{j,\text{en}}$ = droplet generation rate of jth group due to entrainment process
P = pressure
P_B = pressure at projectile base
P'_E, P'_W, P'_S, P'_N = corrected pressures at east, west, south, and north sides of grid
P_e = wetted perimeter
P_∞ = ambient pressure
R = gas constant
R_A = entrainment rate
R^*_P = effective radius of projectile
r = radial direction in cyclindrical coordinate, radius
r_b = regression rate of liquid droplet
r_c = radial distance from centerline to gas–liquid interface
r_d = radius of droplet
r_0 = radius of combustion chamber
S_d = work done by drag force in gas phase
S_{dx}, S_{dr} = drag forces between gas flow and droplets in x, r directions
S_{gx}, S_{gr} = momentum generation rates in x, r directions due to droplet combustion
S_P = pressure work
S_t = work done by shear stress
S_u = source term in pressure correction equation

Received Dec. 20, 1990; revision received May 13, 1991; accepted for publication May 14, 1991.

*Research Associate, Department of Mechanical Engineering. Associate Member AIAA.
†Distinguished Professor, Department of Mechanical Engineering. Fellow AIAA.
‡Professor, Department of Mechanical Engineering.

T_g, T_f, T_s = gas temperature, flame temperature, droplet surface temperature
ΔT = temperature − reference temperature
t, t_0 = time, time at last time step
U_g, $U_{d,k}$ = gas velocity, droplet velocity of kth group droplet in vector form
U_P = projectile velocity
u_c = frontal velocity of Taylor cavity
u_g, u_d = gas velocity, droplet velocity in x direction
u_{pgc} = plasma jet velocity from plasma-generating cartridge
V, ΔV = volume, control volume
v_g, v_d = gas velocity, droplet velocity in r direction
v_w = cavity expansion velocity in r direction
W_{LF}, $W_{LF,C}$ = liquid film flow rate, critical liquid-film flow rate
W_p = projectile mass
X_k = location of kth droplet in vector form
x = x direction in cylindrical coordinate
Y_i = mass fraction of ith species
δ_f = liquid-film thickness
δ_r = engraving depth in projectile
ε = turbulent dissipation energy
η, ζ = new coordinates
θ = angle between rifle line and rotating band
λ_g, λ_{eff} = thermal diffusivity of gas, effective thermal diffusivity
μ_g, μ_T, μ_{eff} = viscosity of gas, turbulent viscosity, effective viscosity ($=\mu_T + \mu_g$)
ρ_e^*, ρ_w^*, ρ_s^*, ρ_n^* = densities at east, west, south, and north sides of grid
ρ_g, ρ_d = gas, droplet density
σ = surface tension
σ_κ, σ_ε = turbulent Prandtl/Schmidt number in κ, ε equations
τ = shear stress, time in new coordinate
ϕ = void fraction
Ψ = dependent variable in Eq. (30)

Subscripts

b = barrel
d = droplet
eff = effective
g = gas
j = jth group of characteristic droplet
k = kth group of characteristic droplet
p = projectile

Superscripts

$=$ = tensor
0 = bulk average
$-$ = time average
$\sim$ = Favre average
$*$ = pseudo-value in finite difference equations
$\rightarrow$ = vector

Introduction

THE electrothermal chemical (ETC) gun is an advanced hypervelocity propulsion concept in which electrical energy from an external power supply is used to heat the working fluid (i.e., liquid propellant) to create thrust for driving a projectile. Tailoring the electrical power input profile allows direct control of energy transfer, from electrical energy to thermal energy and, finally, to projectile kinetic energy in a gun system. Theoretically, it is possible to achieve a constant breech pressure and an optimal muzzle velocity through a suitable power conditioning system for a selected working fluid. Since the projectile kinetic energy is supplied both by the external electrical device and from the chemical energy of the working fluid, the muzzle velocity of an ETC gun is not limited strictly by the size of the gun system. Higher muzzle velocities (usually greater than 2000 m/s) and smaller gun systems can be achieved by tailoring the external electric power source and by selecting an appropriate working fluid.

Some theoretical models have been presented to simulate the interior ballistics of an ETC gun. Oberle[1] used a modified interior ballistic code to investigate the effects of electrical input and working fluids on ETC gun performance. He concluded that ETC guns using an endothermic or exothermic working fluid can exceed the performance of conventional solid-propellant guns. His computational results showed that a 14-mm, 100-caliber ETC gun with a projectile mass of 18 g could achieve a muzzle velocity ranging from 1754 to 2339 m/s, and a ballistic efficiency (defined as the ratio of the projectile kinetic energy to the total input energy) between 10.9% and 12.6% under different operating conditions. Greig et al.[2] applied a simple phenomenological model to predict interior ballistics of the ETC gun under the assumption that 1) plasma mass outside the capillary tube is negligible compared with the mass of gaseous products in the mixing chamber, 2) average temperature in the gun barrel is 3500 K, and 3) projectile acceleration is a function of position in determining pressure distribution in the gun barrel. Results from their theoretical model agree closely with their experimental data.

The theoretical models cited above, though claiming to be capable of predicting the interior processes of an ETC gun, were based on certain artificial approximations without incorporating the actual dynamic motions among the different phases. Thus, the capability of these theoretical models is limited to artificial inputs which remain unknown in most ETC gun systems. It is essential to formulate a multidimensional theoretical model that includes the multiphase dynamic interactions in order to simulate realistically the interior ballistic processes of an ETC gun. The major motivation in the present work is to formulate a comprehensive model and apply suitable numerical techniques for solving this model to predict ETC gun performance.

In this study, a complete set of governing equations is derived from first principles of physics, and a finite difference scheme is employed to discretize the system of governing equations. A staggered grid pattern is used, with the control volume of each grid cell expanding as the projectile travels along the gun barrel. This time-dependent grid structure adequately accounts for the moving boundary effect. The resulting finite difference equations are solved by a modified SIMPLE algorithm[3] at each time step. In this modified algorithm, the pressure-correction equation is subjected to both velocity and density variations. The effect of the latter is related to the pressure correction through use of the Nobel-Abel equation of state.

Theoretical Formulation

The interior ballistic processes of an ETC gun in different stages are shown in Fig. 1. At the beginning of the interior ballistic event, electrical energy from a pulse-forming network (PFN) is discharged into a plasma-generating cartridge (PGC) to generate high-temperature plasma. The plasma jet is led into the gun chamber to interact with the working fluid. A gas cavity, called Taylor cavity, is created within the working fluid due to the plasma jet penetration. The Taylor cavity expands radically and axially as the ETC gun event continues. To study the interior ballistic process of an ETC gun, five distinct regions inside the gun chamber have to be considered. These are the gas phase in the Taylor cavity, the continuous liquid phase near the solid boundary, the dispersed liquid droplet phase, the solid phase including the gun barrel wall and the projectile, and the PGC. The control volume of each

region is illustrated in Fig. 2. The control volume of the gas phase is assumed to be small enough to contain uniform gas properties, yet large enough to include a sufficient number of droplets to make the void fraction continuous. The traditional differential control volume concept is applied to both liquid and solid phases.

Basic Assumptions

1) The flow is axisymmetric.

2) The motions of the large dispersed droplets can be traced in a Lagrangian coordinate system, whereas the small dispersed droplets are assumed to follow the gas motions. The global behavior of the dispersed droplets can be represented by the behavior of finite characteristic groups of droplets and their number densities.

3) The combustion of the liquid propellent is assumed to be the result of burning the oxidizer droplets in a gaseous fuel environment. This assumption is valid since the heat of vaporization of the oxidizer (e.g., H_2O_2/H_2O) is usually higher than that of the liquid propellant (e.g., C_8H_{18}) at standard state (i.e., 2257 kJ/kg for H_2O, 1358 kJ/kg for H_2O_2, and 302 kJ/kg for C_8H_{18}).

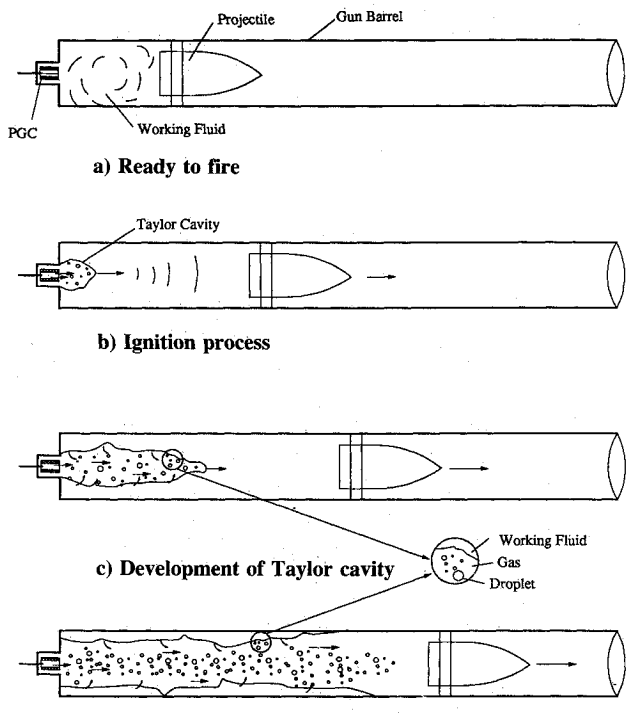

Fig. 1 Schematic of a typical ETC gun firing cycle.

4) The combustion mechanism of the liquid propellant is assumed to follow SCRS (Simple Chemical Reacting System), in which only three distinct species (oxidizer, fuel, and products) exist in a single-step chemical reaction.

5) The body-force term is neglected in the momentum equations.

Governing Equations for Gas Phase

The governing equations for the gas phase are derived for a small control volume containing a large number of dispersed droplets to make the void fraction continuous in space. The concept of Favre averaging and the κ-ε two-equation turbulence model are applied to the transport equations of gas flow. After some manipulation, one can obtain the transport equations[4] governing the mean flow quantities and turbulent fluctuation effects:

Continuity Equation

$$\frac{\partial(\bar{\rho}_g\tilde{\phi})}{\partial t} + \frac{\partial(\bar{\rho}_g\tilde{\phi}\tilde{u}_g)}{\partial x} + \frac{\partial(\bar{\rho}_g\tilde{\phi}\tilde{v}_g)}{r\partial r} = \overline{A_s\bar{r}_b\rho_d} \tag{1}$$

where ϕ is the void fraction representing the volume fraction occupied by the gas, A_s the specific wetted surface area per unit of spatial volume which accounts for the total interfacial area between gas/droplets within the control volume, $\bar{r}_b$ the droplet surface regression rate, and ρ_d the droplet density. Other symbols are defined under "Nomenclature."

x-Momentum Equation

$$\frac{\partial(\bar{\rho}_g\tilde{\phi}\tilde{u}_g)}{\partial t} + \frac{\partial(\bar{\rho}_g\tilde{\phi}\tilde{u}_g\tilde{u}_g)}{\partial x} + \frac{\partial(\bar{\rho}_g\tilde{\phi}\tilde{u}_g\tilde{v}_g r)}{r\partial r} = -\frac{\partial(\bar{P}\tilde{\phi})}{\partial x} + \frac{\partial}{\partial x}\left[\tilde{\phi}\mu_{\text{eff}}\left(\frac{4\partial\tilde{u}_g}{3\partial x} - \frac{2\partial\tilde{v}_g}{3\partial r} - \frac{2\tilde{v}_g}{3r}\right)\right] + \frac{\partial}{r\partial r}\left[\tilde{\phi}\mu_{\text{eff}} r\left(\frac{\partial\tilde{u}_g}{\partial r} + \frac{\partial\tilde{v}_g}{\partial x}\right)\right] - \overline{S_{dx}} + \overline{S_{gx}} \tag{2}$$

where $\overline{S_{dx}}$ represents the drag between the gas flow and droplets in x direction and $\overline{S_{gx}}$ the source due to combustion of droplets which have axial linear momentum. These two terms can be expressed as

$$\overline{S_{dx}} = \overline{D_{t,x}A_s} \tag{3}$$

$$\overline{S_{gx}} = \overline{A_s\bar{r}_b\rho_d u_d} \tag{4}$$

where $D_{t,x}$ is the total drag force in the x direction due to relative motion between gas and droplet phases.[5]

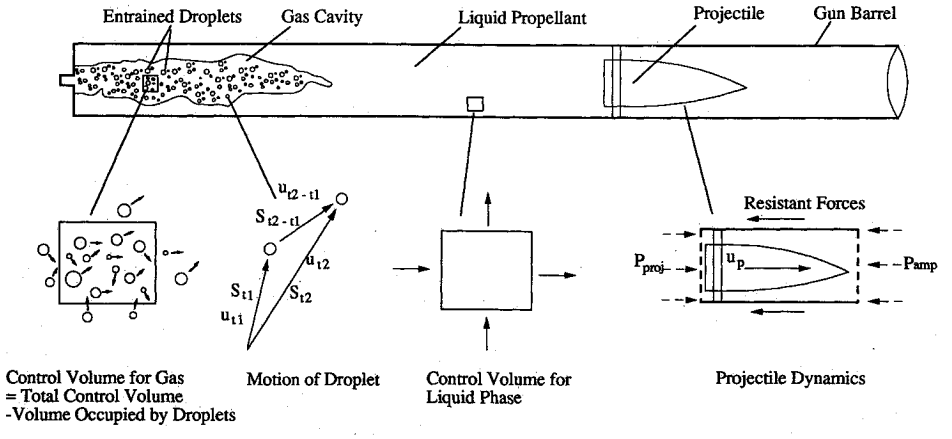

Fig. 2 Control volumes for different regions in an ETC gun.

r-Momentum Equation

$$\frac{\partial(\overline{\rho_g}\tilde{\phi}\tilde{v}_g)}{\partial t} + \frac{\partial(\overline{\rho_g}\tilde{\phi}\tilde{v}_g\tilde{u}_g)}{\partial x} + \frac{\partial(\overline{\rho_g}\tilde{\phi}\tilde{v}_g\tilde{v}_g r}{r\partial r} = -\frac{\partial(\overline{P\phi})}{\partial r} + \frac{\partial}{\partial x}\left[\tilde{\phi}\mu_{\text{eff}}\left(\frac{\partial\tilde{u}_g}{\partial r} + \frac{\partial\tilde{v}_g}{\partial x}\right)\right] - \overline{S_{dr}} + \overline{S_{gr}} + \frac{\partial}{r\partial r}\left[\tilde{\phi}\mu_{\text{eff}} r\left(\frac{4}{3}\frac{\partial\tilde{v}_g}{\partial r} - \frac{2}{3}\frac{\tilde{v}_g}{r} - \frac{2\partial\tilde{u}_g}{3\partial x}\right)\right] + \frac{\mu_{\text{eff}}}{r}\left(\frac{4}{3}\frac{\tilde{v}_g}{r} - \frac{2\partial\tilde{v}_g}{3\partial r} - \frac{2\partial\tilde{u}_g}{3\partial x}\right) \tag{5}$$

Energy Equation

$$\frac{\partial(\overline{\rho_g}\tilde{\phi}\tilde{H})}{\partial t} + \frac{\partial(\overline{\rho_g}\tilde{\phi}\tilde{H}\tilde{u}_g)}{\partial x} + \frac{\partial(\overline{\rho_g}\tilde{\phi}\tilde{H}\tilde{v}_g r)}{r\partial r} = \frac{\partial}{\partial x}\left[\tilde{\phi}\lambda_{\text{eff}}\left(\frac{\partial\tilde{T}_g}{\partial x}\right)\right] + \frac{\partial}{r\partial r}\left[r\tilde{\phi}\lambda_{\text{eff}}\left(\frac{\partial\tilde{T}_g}{\partial r}\right)\right] + \overline{\dot{q}_d} - \overline{\dot{q}_{ht}} - \overline{S_P} - \overline{S_t} - \overline{S_d} - \overline{P\frac{\partial\phi}{\partial t}} \tag{6}$$

where H represents total energy, $\overline{\dot{q}_d}$ energy released rate from droplet combustion, $\overline{\dot{q}_{ht}}$ rate of energy transferred from the gas flow to droplets, $\overline{S_d}$ energy loss rate due to drag force between droplets and gas flow, $\overline{S_t}$ dissipation energy, and $\overline{S_P}$ compressible work due to void fraction. The terms on the RHS of Eq. (6) can be expressed as

$$\overline{\dot{q}_d} = \left\langle \overline{A_s\bar{r}_b\rho_d}\left(\Delta h_d + \frac{1}{2}\tilde{u}_d|\tilde{u}_d| + \frac{1}{2}\tilde{v}_d|\tilde{v}_d|\right)\right\rangle \tag{7}$$

$$\overline{\dot{q}_{ht}} = \langle\overline{A_s}(h_{\text{conv},d} + h_{\text{rad},d})(\tilde{T}_g - \tilde{T}_{ds})\rangle \tag{8}$$

$$\overline{S_d} = \langle(D_{t,x}|\tilde{u}_g - \tilde{u}_d| + D_{t,r}|\tilde{v}_g - \tilde{v}_d|)\overline{A_s}\rangle \tag{9}$$

$$\overline{S_t} \equiv \overline{\nabla\cdot(\bar{\bar{\tau}}\tilde{U}_g)} \tag{10}$$

$$\overline{S_P} = \left\langle\frac{\partial(\overline{P\phi})}{\partial t} + \overline{u_g\frac{\partial(P\phi)}{\partial x} + v_g\frac{\partial(P\phi)}{\partial r} - P\frac{\partial\phi}{\partial t}}\right\rangle \tag{11}$$

In most cases the dissipation term is negligible compared to the heat release term.

Diffusion Equation

$$\frac{\partial(\overline{\rho_g}\tilde{\phi}\tilde{Y}_i)}{\partial t} + \frac{\partial(\overline{\rho_g}\tilde{\phi}\tilde{Y}_i\tilde{u}_g)}{\partial x} + \frac{\partial(\overline{\rho_g}\tilde{\phi}\tilde{Y}_i\tilde{v}_g r)}{r\partial r} = \frac{\partial}{\partial x}\left(\overline{\rho_g}\tilde{\phi}D_{\text{eff}}\frac{\partial\tilde{Y}_i}{\partial x}\right) + \frac{\partial}{r\partial r}\left(\overline{\rho_g}\tilde{\phi}D_{\text{eff}}r\frac{\partial\tilde{Y}_i}{\partial r}\right) + \overline{\dot{m}_i} \tag{12}$$

Equation of State

$$\overline{P} = b\overline{\rho_g}\tilde{P} + R\overline{\rho_g}\tilde{T}_g \tag{13}$$

which is an alternative form of the Noble-Abel equation, $P(1/\rho_g - b) = RT_g$.

Turbulence Model

κ Equation

$$\frac{\partial(\overline{\rho_g}k)}{\partial t} + \frac{\partial(\overline{\rho_g}\tilde{u}_g k)}{\partial x} + \frac{\partial(\overline{\rho_g}\tilde{v}_g kr)}{r\partial r} = \frac{\partial}{\partial x}\left[\left(\frac{\mu_T}{\sigma_k} + \mu_g\right)\frac{\partial k}{\partial x}\right] + \frac{\partial}{r\partial r}\left[r\left(\frac{\mu_T}{\sigma_k} + \mu_g\right)\frac{\partial k}{\partial r}\right] + G_k - \frac{\mu_T}{\overline{\rho_g^2}}\frac{\partial\overline{\rho_g}}{\partial r}\frac{\partial\bar{P}}{\partial r} - \frac{\mu_T}{\overline{\rho_g^2}}\frac{\partial\overline{\rho_g}}{\partial x}\frac{\partial\bar{P}}{\partial x} - \overline{\rho_g}\varepsilon + \overline{A_s\bar{r}_b\rho_d}k \tag{14}$$

where μ_T is the turbulent viscosity.

ε Equation

$$\frac{\partial(\overline{\rho_g}\varepsilon)}{\partial t} + \frac{\partial(\overline{\rho_g}\tilde{u}_g\varepsilon)}{\partial x} + \frac{\partial(\overline{\rho_g}\tilde{v}_g\varepsilon r)}{r\partial r} = \frac{\partial}{\partial x}\left[\left(\frac{\mu_T}{\sigma_\varepsilon} + \mu_g\right)\frac{\partial\varepsilon}{\partial x}\right] + \frac{\partial}{r\partial r}\left[r\left(\frac{\mu_T}{\sigma_\varepsilon} + \mu_g\right)\frac{\partial\varepsilon}{\partial r}\right] + C_{\varepsilon 1}\frac{\varepsilon}{k}\left(G_k + \frac{\mu_T}{\overline{\rho_g^2}}\frac{\partial\overline{\rho_g}}{\partial r}\frac{\partial\bar{P}}{\partial r} - \frac{\mu_T}{\overline{\rho_g^2}}\frac{\partial\overline{\rho_g}}{\partial x}\frac{\partial\bar{P}}{\partial x}\right) - C_{\varepsilon 2}\overline{\rho_g}\frac{\varepsilon^2}{k} + \overline{A_s\bar{r}_b\rho_d}\varepsilon \tag{15}$$

where G_k is expressed as

$$G_k \equiv \frac{4}{3}\mu_T\left[\left(\frac{\partial\tilde{u}_g}{\partial x}\right)^2 - \frac{\partial\tilde{u}_g}{\partial x}\left(\frac{\partial\tilde{v}_g}{\partial r} + \frac{\tilde{v}_g}{r}\right)\right] + \left(\frac{\partial\tilde{v}_g}{\partial r} + \frac{\tilde{v}_g}{r}\right)^2 + \mu_T\left(\frac{\partial\tilde{u}_g}{\partial r} + \frac{\partial\tilde{v}_g}{\partial x}\right)^2 - \frac{2}{3}\overline{\rho_g}k\left(\frac{\partial\tilde{u}_g}{\partial x} + \frac{\partial\tilde{v}_g}{\partial r} + \frac{\tilde{v}_g}{r}\right) \tag{16}$$

The last terms in both Eqs. (14) and (15) represent the effect of gas generation due to the burning of droplets.

The boundary conditions for the gas phase at the centerline can be given in the following form due to line symmetry conditions

$$@\ r = 0,\quad 0 \le x \le L_c$$

$$\frac{\partial\tilde{u}_g}{\partial r} = 0,\quad \frac{\partial\tilde{v}_g}{\partial r} = 0,\quad \frac{\partial\tilde{T}_g}{\partial r} = 0,\quad \frac{\partial k}{\partial r} = 0,\quad \frac{\partial\varepsilon}{\partial r} = 0 \tag{17}$$

Some important points need be stressed in the specification of boundary conditions at the interface of plasma/working fluid. Due to the extremely high heat transfer rate from the plasma jet, a very thin liquid layer near the interface can be heated up to high temperatures. In the meantime, the entrainment rate is very large as a result of high plasma jet velocity relative to the working fluid. The thin heated liquid layer can be entrained off instantly to expose the subcooled working fluid region. As the PFN discharge process continues, the working fluid becomes thinner and thinner. Resulting from the entrainment at the interface, the gas cannot depart from the liquid surface at a high blowing velocity as in conventional pyrolysis cases. Therefore, the gas velocity at the interface is equal to the cavity radial expansion velocity v_w, which can be derived from the change of overall working fluid volume. Similarly, the shear flow velocity at the interface of gas/working fluid can be considered negligible. Furthermore, the gas-phase temperature gradient at the interface can be treated nearly adiabatic because the motion of entrained par-

ticle creates extensive mixing of surrounding gases. As a result, the boundary conditions can be expressed as

$$@\ r = r_c,\quad 0 \le x \le L_c$$

$$\tilde{u}_g = 0,\quad \tilde{v}_g = v_w,\quad k = \varepsilon = 0,\quad \frac{\partial \tilde{T}_g}{\partial r} \doteq 0 \tag{18}$$

At the breech end, the boundary conditions can be specified as

$$@\ x = 0,\quad 0 < r < r_c$$

$$\tilde{u}_g = \tilde{u}_{pgc},\quad \tilde{v}_g = 0,\quad \frac{\partial \tilde{T}_g}{\partial x} = 0,\quad \frac{\partial k}{\partial x} = -\frac{C_\mu \rho_g k^2}{\mu_T u_g},$$

$$\frac{\partial \varepsilon}{\partial x} = -\frac{C_{\varepsilon 2} C_\mu \rho_g k \varepsilon}{\mu_T u_g} \tag{19}$$

At the Taylor cavity front, the boundary conditions can be specified as

$$@\ x = L_c,\quad 0 < r < r_c$$

$$\tilde{u}_g = \tilde{u}_c \quad \text{or} \quad = \tilde{u}_p,\quad \tilde{v}_g = 0,\quad \frac{\partial k}{\partial x} = 0,$$

$$\frac{\partial \varepsilon}{\partial x} = 0,\quad \frac{\partial \tilde{T}_g}{\partial x} \doteq 0 \tag{20}$$

where u_{pgc} is the high-temperature gas velocity from the injector exit of the PGC determined by the pressure difference between the PGC and gun chamber, u_c is the Taylor cavity frontal velocity, u_p is the projectile velocity, and v_w is the radial expansion velocity of cavity. The quantities v_w, u_c, and u_p are determined from the system of equations as part of the solution. Note that boundary conditions for κ and ε at $x = 0$ are based on the limiting forms of κ and ε equations under freestream conditions, with $C_\mu = 0.09$ and $C_{\varepsilon 2} = 1.89$.[6]

Governing Equations for Dispersed Droplets

The equations of motion for the large droplets of the kth group in the Lagrangian coordinate system can be written as[7]

$$\frac{\pi d_{d,k}^3 \rho_d}{6} \frac{d(\vec{U}_{d,k})}{dt} = \frac{\pi}{8} d_{d,k}^2 \rho_g C_{D,k} |\vec{U}_g - \vec{U}_{d,k}| (\vec{U}_g - \vec{U}_{d,k}) - \frac{\pi}{6} d_{d,k}^3 \nabla P \tag{21}$$

$$\frac{d(\vec{X}_k)}{dt} = \vec{U}_{d,k} \tag{22}$$

where $\boldsymbol{X}_k$ and $\boldsymbol{U}_{d,k}$ are the position and velocity of the representative droplet in the kth group large droplet. The first term on the RHS of Eq. (21) represents the interfacial drag effect, whereas the second term denotes the pressure gradient effects.

The small droplets ($d_d < 45\ \mu$m) are considered to follow the gas flow motions,[8] i.e., the droplet velocity is equal to the local gas velocity. The droplet number density equation for the jth group small droplets can then be written as

$$\frac{\partial (n_j)}{\partial t} + \frac{\partial (n_j u_g)}{\partial x} + \frac{\partial (n_j v_g r)}{r \partial r} = -C_{1,j} n_j + \sum_{i=j+1} C_{2,i} n_j + \dot{n}_{j,\text{en}} \tag{23}$$

where the first term on the RHS represents the decrease of droplet number density of the jth group due to burning, the second term the increase of number density due to larger droplets converting into the size of the jth group as a result of burning, and the last term the increase of number density resulting from the entrainment process. Note that liquid entrainment represents the major consequence of the plasma/working fluid interaction. Because high gas velocity prevails in most of the interior ballistic event, only a small number of large droplets are generated by entrainment. The effect of relative motions between large droplets and gas flow is considered insignificant. Therefore, in this work, six groups of droplets, with characteristic sizes ranging from 20 to 200 μm, are employed to represent all dispersed droplets. Six separate droplet number-density equations are solved to calculate the droplet number for each group in order to determine the total droplet volume and the void fraction.

The liquid entrainment in an ETC gun firing cycle is considered to be attributed mainly to the roll wave entrainment mechanism (i.e., Helmholtz instability). An analysis of Helmholtz instability based on the thin liquid film assumption, rather than on the conventional semi-infinite liquid medium assumption, is applied to estimate the droplet-size distribution when generated by entrainment.[9] The result is

$$\left(\frac{d_d}{d_t}\right)\left(\frac{\rho_g u_g^{o2} d_t}{\sigma}\right)^{1/2} = C_1 \left(\frac{\delta_f}{d_t}\right)^{1/2} \left(\frac{f_s}{f_f}\right)^{1/2} \tag{24}$$

where d_d is the characteristic droplet size, u_g^o the bulk gas velocity, σ the surface tension, d_t the hydraulic diameter of the tube, f_s the friction factor for a smooth pipe, f_f the friction factor for a rough pipe, δ_f the liquid film thickness, and C_1 a coefficient inversely proportional to the square root of f_s.

In order to determine the characteristic droplet diameter, d_d is first expressed in terms of a droplet-size distribution function. By applying the experimental data and the volume distribution function, Tatterson et al.[9] obtained the expression for characteristic droplet diameter as

$$\frac{d_{32}}{d_t}\left(\frac{\bar{\rho}_g u_g^{o2} f_s d_t}{2\sigma}\right)^{1/2} = 0.023 \tag{25}$$

where d_{32} represents the Sauter mean diameter.

The entrainment rate in this study neglects the deposition of droplets into the liquid phase because droplet lifetime is very short in a high-temperature environment. The droplets have very little chance to return to the liquid film before they completely burn out. The atomization rate from the liquid film is suggested by Dallaman[10] from experimental data

$$R_A = K_A \left[\frac{W_{LF} - W_{LF,C}}{P_e}\right] u_g^{o2} (\bar{\rho}_g \bar{\rho}_1)^{1/2} \tag{26}$$

where $W_{LF,C}$ is the critical liquid mass flow rate required for initiating atomization at the bulk gas velocity u_g^o, the wetted perimeter P_e, and the dimensional atomization rate constant K_A. Dallaman also suggested values of $K_A = 3.5 \times 10^{-6}$ s^2/kg, $W_{LF,C}/P_e = 0.046$ kg/m/s for an air–water flow in a vertical pipe.

The droplet burning rate in the gaseous flow is expressed for a droplet burning in a quiescent environment[8] as

$$\dot{m}_d = \frac{4\pi r_d \lambda_g}{C_{Pg}} \ln\left[1 + \frac{C_{Pg}(T_f - T_s)}{\Delta H_{fg}}\right] \tag{27}$$

where $\dot{m}_d$ is the droplet burning rate, ΔH_{fg} the sum of the latent heat and sensible heat, and λ_g the thermal conductivity of gas. Due to the fact that pressure and temperature inside the combustion chamber of the ETC gun are very high, the

boundary conditions at the droplet surface are considered to be near the critical point.

Governing Equations for Projectile Dynamics and Liquid Phase

The projectile motion proceeds under the influence of two types of forces: propulsive and resistive. As suggested by Fisher and Trippe,[11] the total resistant force consists of 1) force required for engraving the rotating band, 2) drag resistant force from the projectile motion through the barrel where a metal–metal press fit situation exists, 3) propulsive forces used for angular acceleration, and 4) frictional sliding resistance from the resolved force normal to the edge of the band. The driving force is the result of the chamber pressure acting on the projectile base.

By balancing the driving force and resistive forces on the free body diagram of the projectile, one can express the projectile acceleration as

$$a_P = \frac{R_P^*[(P_B - P_\infty)A_{CS}(\cos\theta - C_f\sin\theta) - F_D']}{W_pR_P^*(\cos\theta - C_f\sin\theta) + I_PK_P(\cos\theta + C_f\sin\theta)} \tag{28}$$

where P_∞ is the ambient pressure, and W_p the mass of the projectile. Projectile velocity, projectile travel distance, and muzzle velocity can then be determined from the projectile acceleration.

The liquid phase, which includes the liquid film along the gun barrel wall and the liquid column behind the projectile base, is governed by a system of continuity, momentum, and energy equations (see Chen[4]). The liquid phase is assumed to follow the projectile, i.e., there is no detachment between the working fluid and the projectile base. As such, the liquid column driven by the cavity front moves at the velocity of the projectile. To facilitate the solution, the liquid film thickness near the gun barrel wall is assumed be a strong function of time but a weak function of the axial location. Once the projectile location and gas cavity size are determined, the motion and geometry of the liquid phase can be calculated through simple physical relationships.

The PGC is treated as a zero-dimensional lump system because the dimension is small compared to that of the gun chamber. This lump system can be viewed as a source located directly behind the breech to provide plasma jet to the gun chamber. The plasma generation rate inside the PGC can be determned as long as the PFN discharge power and plasma thermochemical properties are known. The PGC pressure can be calculated by the use of the continuity equation and the equation of state. Based on the gas dynamic relations and the pressures at the PGC and the gun chamber, the plasma injection rate can be specified. The plasma injection velocity serves as a boundary condition for the gas phase.

Numerical Methods

The gas phase inside the gun chamber expands during the firing cycle as a result of projectile motion, as does the computational domain of the gas phase. The computational domains of the gas phase at different stages are shown in Fig. 3. Initially, only a small cavity exists within the working fluid (Fig. 3a). As plasma penetration continues and the projectile travels forward, this cavity expands in radial and axial directions (Fig. 3, b and c). After all working fluid is entrained into the cavity, the gaseous region expands only in the axial direction. In this study, a fixed number of computational grid points are employed. The grid sizes, therefore, increase as the projectile travels through the gun barrel (i.e., the grid dimensions are functions of time). A few set of time-dependent coordinates, τ, η, and ζ, is introduced to accommodate the effect of grid-size expansion. These new coordinates are defined as

$$\tau = t, \quad \eta = x + u_c(t - t_0), \quad \zeta = r + v_w(t - t_0) \tag{29}$$

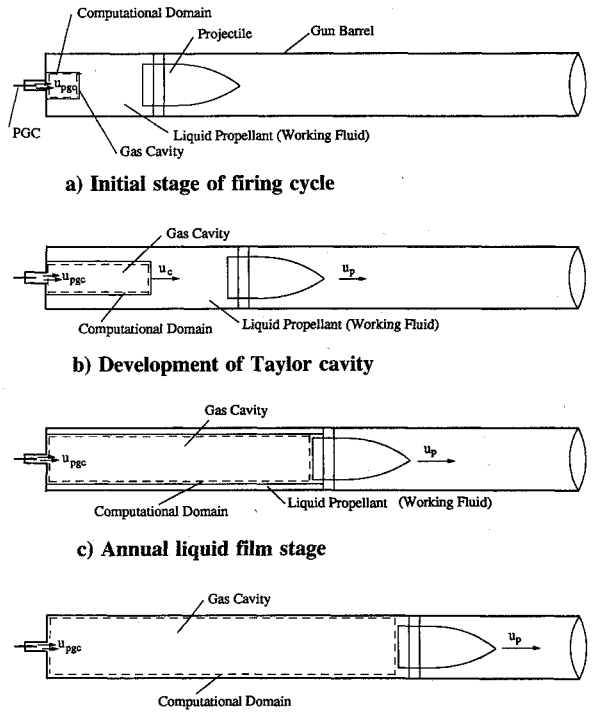

Fig. 3 Gas-phase computational domains in various stages of the firing cycle.

where u_c and v_w represent the frontal velocity and radial expansion velocity of the Taylor cavity, respectively. By taking the derivatives of the new coordinates (τ, η, and ζ) with respect to the old ones (t, x, and r), it can be shown that only the unsteady terms in the governing equations are affected by expansion of the computational domain. The relationship between the new and original coordinates for the unsteady terms is

$$\frac{\partial(\Phi\psi\rho_g)}{\partial t} = \frac{\partial(\Phi\psi\rho_g)}{\partial\tau} + u_c\frac{\partial(\Phi\psi\rho_g)}{\partial\eta} + v_w\frac{\partial(\Phi\psi\rho_g)}{\partial\zeta} \tag{30}$$

where ψ is one of the dependent variables in the governing equations, with $\psi = 1$, u_g, v_g,and H for the continuity, x momentum, r momentum, and energy equation, respectively.

The SIMPLE algorithm is used to solve the finite difference equation in the gas phase. In the SIMPLE algorithm, the pressure distribution is estimated first. Accurate distribution of pressure is then calculated from the pressure-correction equation to update the value. In the original SIMPLE algorithm, this pressure-correction equation is obtained by combining the continuity and momentum equations, and only under the influence of u_g, v_g velocities. For highly compressible flows, however, the flow density distribution contributes significantly to the pressure distribution. The density variation effect, together with the flow velocity, must be included in the pressure-correction equation. By introducing a suitable equation of state, the pressure-correction equation can be modified as

$$a_PP_P' = a_EP_E' + a_wP_w' + a_NP_N' + a_SP_S' + S_u \tag{31}$$

with

$$a_E = (\rho_e^*d_e - Ku_e^*)A_\eta$$

$$a_W = (\rho_w^*d_w - Ku_w^*)A_\eta$$

$$a_S = (\rho_s^*d_s - Ku_s^*)A_\zeta$$

$$a_N = (\rho_n^*d_n - Ku_n^*)A_\zeta$$

$$a_P = (\rho_n^*d_n + \rho_s^*d_s)A_\zeta + (\rho_e^*d_e + \rho_w^*d_w)A_\eta + \frac{K\Delta V}{\Delta t}$$

where superscript * is the pseudo-value. Note that K represents the effects of density variation on local pressure at a fixed temperature, obtained by taking the derivative of density with respect to pressure at constant temperature in equation of state. Employing the Noble-Abel equation of state, the variable K can be expressed as

$$K = \frac{RT_g}{(Pb + RT_g)^2} \tag{32}$$

where R and b are the gas constant and covolume, respectively.

Results and Discussion

The ETC gun system considered in this work is a 25-mm, 100-caliber gun with a combustion chamber of 45.05 cc (length/diameter = 3.5). The working fluid is a mixture of C_8H_{18}/H_2O_2 (with C_8H_{18} 25% by volume). This working fluid has the impetus of 1694.5 kJ/kg and can release chemical energy of 6458 kJ/kg.[1] The projectile weights 70 g. Detailed information on the gun system is summarized in Table 1.

Various sets of PFN discharge curves are applied to study their effects on ETC gun performance. The characteristic curve of the power discharge process of PFN has a sawtooth shape, with electrical power increasing linearly at the beginning to maximum discharge power, and then decreasing linearly to zero at the end. PFN discharge processes are designed to have different total discharge times and peak power times, as shown in Figs. 4a and 4b, respectively. In Fig. 4a, the peak discharge power occurs at four different times: 0.8, 1.0, 1.4, and 1.8 ms, whereas the total discharge time is fixed at 2.0 ms. In Fig. 4b, three different peak power times, 1.2, 1.4, and 1.8 ms, occur at three different total discharge times, 1.4, 1.6, and 2.0 ms, respectively.

Model Validation

The theoretical model is validated by comparing it with available experimental data. To achieve this, the measured breech pressure-time trace at FMC[12] for a 30-mm CAP gun (one type of electrothermal chemical gun) with Test No. CAP48 is employed. The predicted breech pressure-time traces for three typical PFN discharge characteristics (PFN peak power time/discharge time of 1.4 ms/2.0 ms, 1.4 ms/1.6 ms, and 1.0 ms/2.0 ms) are compared with the measured breech pressure-time trace in Fig. 5. The measured breech pressure-time trace exhibits double peaks in the first half of the event. The first peak, with a value of 276 MPa, occurs at 0.36 ms; the second peak, with a value of 325 MPa, occurs at 0.6 ms. After reaching the second peak, the measured breech pressure continues to decrease until the end of the event (2 ms). The predicted breech pressure-time histories also show a similar trend, with double peaks in the early stage. Although the predicted first peaks in all three cases are smaller than the one measured, all of the four first peaks occur almost at the same time. The predicted second peaks (maximum breech pressure) of these three cases are 340, 359, and 395 MPa, respectively, slightly greater (4.6%, 10.8%, and 21.5%) than the measured second peak pressure. The predicted second peaks at 0.66, 0.63, and 0.61 ms, respectively, are also very close to the one measured. Overall, the predicted results agree favorably with the experimental data.

Table 1 Input information for a 25-mm 100-caliber ETC Gun

Gun system	
Chamber dimension	2.54 cm (D) × 8.89 cm (L), 45.05 cm³
Injector exit diameter	0.76 cm (0.3″)
Capillary tube volume	10.39 CC
Shot start pressure	3.6 × 10⁷ PA
Initial Taylor cavity diameter	1.295 cm (0.51″)
Initial ullage	5% (by volume)
Projectile mass	70 g
Working fluid[a]	
Composition	C_8H_{18}/H_2O_2(25%/75% by vol)
Impetus	1694.5 kJ/kg
Chemical energy	6458 kJ/kg
Density	1260 kg/m³
Heat of evaporation at 1 atm, 298 K	928.33 kJ/kg
Gaseous product[a]	
Molecular weight	16.8441
Specific heat	2366.1 J/kg-K
Covolume	1.058 × 10⁻³ m³/kg

[a]Based on the data reported by Oberle.[1]

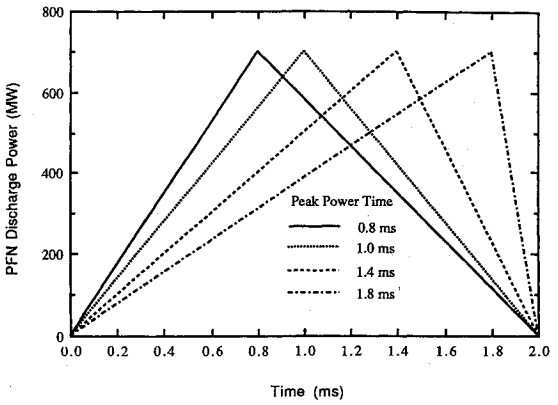

a) Various peak power times

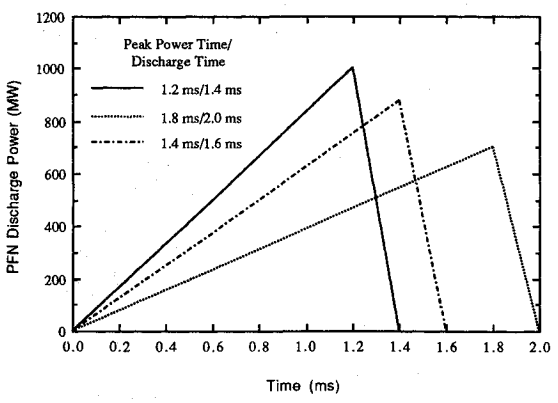

b) Various total discharge times

Fig. 4 PFN Discharge power curves with a) various peak power times b) various total discharge times.

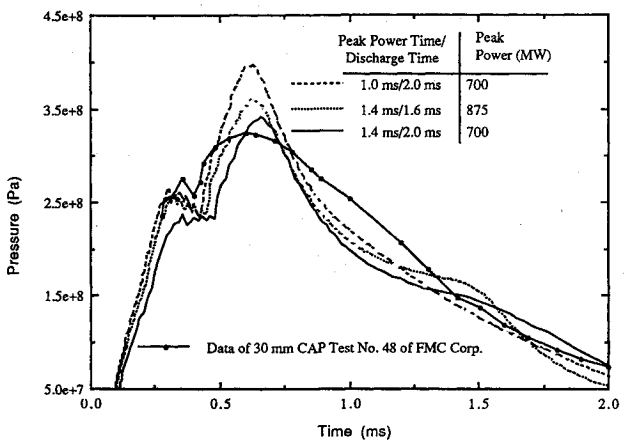

Fig. 5 Comparison of the predicted breech pressure-time traces with the FMC data.

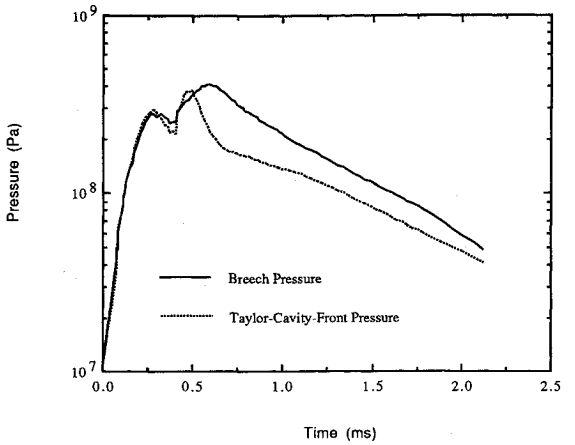

Fig. 6 Breech and Taylor cavity front pressures-time traces for the case with a PFN discharge time of 2.0 ms and a peak power time of 0.8 ms.

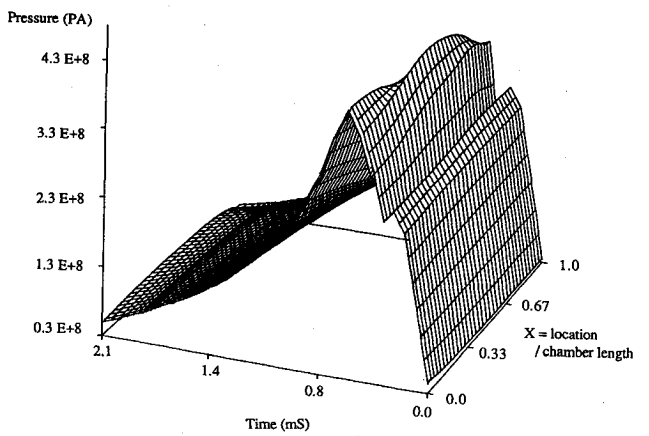

Fig. 7 Time history of averaged axial pressure in the ETC gun chamber with a PFN discharge time of 2.0 ms and a peak power time of 0.8 ms.

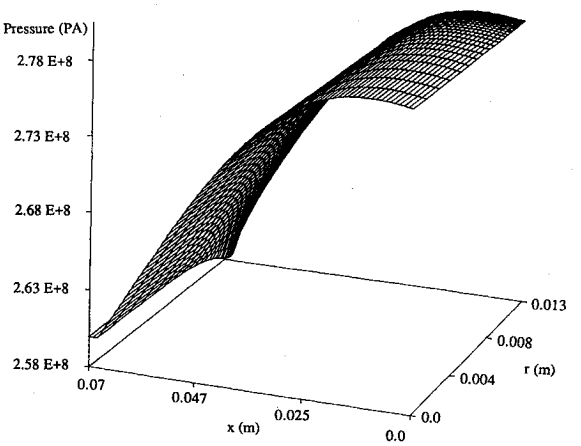

Fig. 8 Spatial pressure distribution in the ETC gun chamber at 0.33 ms with a PFN discharge time of 2.0 ms and a peak power time of 0.8 ms.

PFN Discharge Curve with a Discharge Time of 2.0 ms and a Peak Power Time of 0.8 ms

Computed pressure-time traces at the breech and Taylor cavity front obtained from a typical PFN discharge curve are shown in Fig. 6. These two pressure-time traces are similar in shape; both have two peaks at the beginning, with the first peak occurring at almost the same time and magnitude (0.3 ms, 270 MPa). A valley follows the first peak, then both

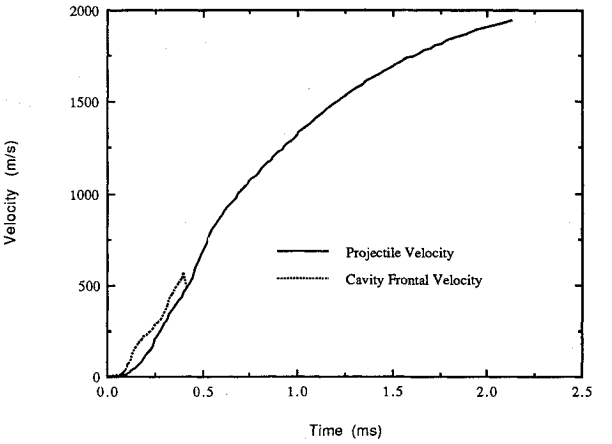

Fig. 9 Projectile and Taylor cavity frontal velocities-time traces with PFN a discharge time of 2.0 ms and a peak power time of 0.8 ms.

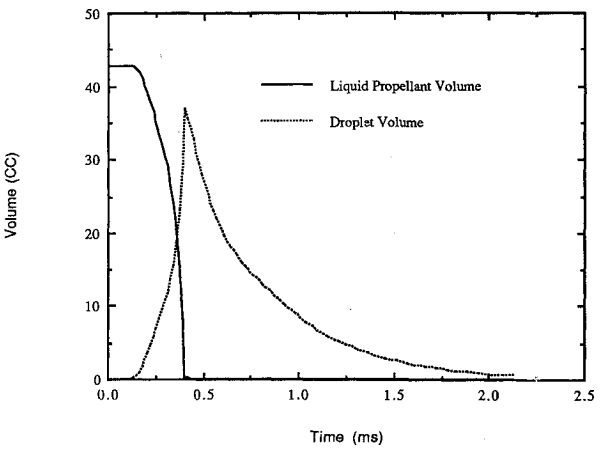

Fig. 10 Liquid propellant and droplet volumes-time traces with a PFN discharge time of 2.0 ms and a peak power time of 0.8 ms.

pressure traces rise to reach the second peaks. After the second peak, the pressures gradually decrease toward the end of the event. Before the first peak, pressures at the breech and Taylor cavity front are almost identical. In this stage, pressurization is controlled by the plasma discharging processes. The chamber pressure builds up quickly over the shot-start pressure to initiate the projectile motion. Once the projectile starts to move, the chamber volume and gas cavity expand. However, both the amount of gaseous products generated through chemical reactions and the flow rate of the plasma jet are not high enough to maintain chamber pressure during the chamber volume expansion. As a result, the chamber pressure decreases quickly to the valley (0.4 ms) in the pressure-time trace.

Three factors may contribute to the second peak pressure. As the process continues, more working fluid is entrained into the gas cavity; thus, chemical reactions of entrained droplets release more amounts of gas products. Also, the plasma jet from the PGC becomes stronger due to a higher PFN discharge power. These two factors bring up the chamber pressure. The dynamic motion of the cavity (i.e., the frontal velocity) also plays an important role in formation of the second peak pressure. The frontal velocity is greater than the projectile velocity at this point becaues the cross-sectional area of the Taylor cavity is less than that of the gun barrel. Finally, the cavity front will catch up the projectile and move with it. The frontal velocity of the Taylor cavity reduces to that of the projectile after the cavity front hits the projectile base. This also contributes to the pressure rise to form the second peak at the front of Taylor cavity (390 MPa at 0.5 ms). This pressure wave front then travels back to the gun breech at approximately 0.6 ms.

The calculated interior ballistic event, beginning with the initial PFN discharge and ending as the projectile leaves the gun muzzle, takes approximately 2.12 ms. Detailed pressure wave propagation and motions inside the chamber during the interior ballistic events can be seen in Fig. 7, which shows radially averaged chamber pressure distribution along the axis at various time steps during the event. Before 0.3 ms the pressure gradient inside the cavity is small, but the pressure wave builds up quickly to reach the first peak. After reaching the valley (at 0.4 ms), pressure at the projectile base ($x = 1$) starts to increase. The pressure wave front can be clearly seen propagating from the projectile base to the breech ($x = 0$), and bouncing back. The chamber pressure decreases continuously as the projectile accelerates in the downstream direction. The spatial (two-dimensional) chamber pressure distribution at 0.33 ms is shown in Fig. 8. At this particular moment, the pressure gradient in the axial direction is greater than that in the radial direction. Because of the relatively large magnitudes of the pressure, the radial variation is not discernible in the figure.

Projectile velocity and cavity frontal velocity time histories are shown in Fig. 9. Muzzle velocity is 1936 m/s at 2.11 ms, which gives a ballistic efficiency of 12%, with an electrical energy input of 0.7 MJ and a chemical energy release of approximately 0.4 MJ. The projectile motion is driven by the projectile base pressure; therefore, acceleration of the projectile is highest around 0.5 ms, where the projectile base pressure reaches its peak value. Before 0.4 ms, frontal velocity of the Taylor cavity is greater than projectile velocity. In this stage, the Taylor cavity develops within the working fluid with a volumetric expansion rate equal to that of the gun chamber. Since the cavity diameter is smaller than the combustion chamber diameter, the cavity front moves at a greater velocity ranging from 50 to 100 m/s. As the cavity expands, the cavity front moves closer and closer to the projectile base. Finally, the cavity front hits the projectile base at 0.4 ms; after that, the cavity frontal velocity is equal to the projectile velocity. Time histories of total volumes occupied by working fluid and droplets are shown in Fig. 10. The entrainment process of the working fluid is not obvious before 0.15 ms. After 0.15 ms, the gas flow velocity reaches a critical value to begin efficient entrainment. The volume of the working fluid drops drastically, and droplet volume and number density increase quickly at the same time. More droplets provide more burning surface area to generate more gaseous products. As a result, both chamber pressure and gas dynamic motion build up quickly for extensive entrainment. The entrainment process continues until all the working fluid is transformed into droplets; this occurs at 0.41 ms.

PFN Discharge Curve with a Discharge Time of 1.6 ms and a Peak Power Time of 1.4 ms

The time histories of pressure at the breech and the Taylor cavity front for a discharge duration of 1.6 ms and a peak power time of 1.4 ms are shown in Fig. 11. The overall configurations of these two pressure-time traces are similar to those exhibited in the previous case. Comparing the first pressure peak with the previous case (289 MPa at 0.29 ms), this case has a slightly smaller value of 261 MPa at 0.33 ms. This lower initial pressurization process is a result of weaker plasma jet velocity subject to a weaker initial PFN discharge process. A second peak in the pressure-time trace occurs at 0.63 ms at the breech, with a value of 359 MPa. Compared to the previous case (Fig. 6), the chamber pressure in this case shows a slower decrease after the second peak because more plasma jet is generated in the later stage to boost breech pressure. The pressure trace at the breech shows a small hump at around 1.5 ms because the peak PFN discharge power appears at 1.4 ms. This pressure wave travels from the breech to the projectile base at 1.7 ms and creates a small hump in the pressure trace at the projectile base (which is also the cavity front in this stage). After this hump appears, pressure at the breech drops quickly after 1.6 ms because plasma generation rate decreases rapidly in the PGC. Note that a small positive pressure gradient in the combustion chamber appears at the end of the event, different from the previous case when the peak PFN discharge point is located in the first-half time period. A comparison with the pressure-time traces in the second-half stage (after 1 ms) shows that pressure traces at the breech and projectile base in this case remain a constant longer, a situation more desirable for gun performance. It can be concluded that the characteristics of PFN discharge processes have important effects on the interior ballistic processes of an ETC gun. This is discussed further in subsequent sections.

Effects of PFN Discharge Peak Power Time on Interior Ballistics

The effects of peak power time in the PFN discharge process are discussed in this section. Four sets of PFN discharge curves with the same total discharge time (2.0 ms) and total electrical energy (0.7 MJ), but with four different peak power times (0.8, 1.0, 1.4, and 1.8 ms) shown in Fig. 4, are employed.

The pressure-time traces at the breech for these four cases are shown in Fig. 12. All exhibit a similar trend in the first-half stage, having double peaks with a valley in between. As the peak power time advances, the first peak value moves higher and its corresponding time earlier (i.e., 230 MPa at 0.43 ms and 289 MPa at 0.29 ms for the peak power time at 1.8 and 0.8 ms, respectively). The early peak power time indicates that a stronger plasma jet is generated in the early stage. This strong plasma jet is helpful in initial pressurization, increasing both chamber pressure and cavity frontal velocity. As a result, a higher second peak pressure is generated for

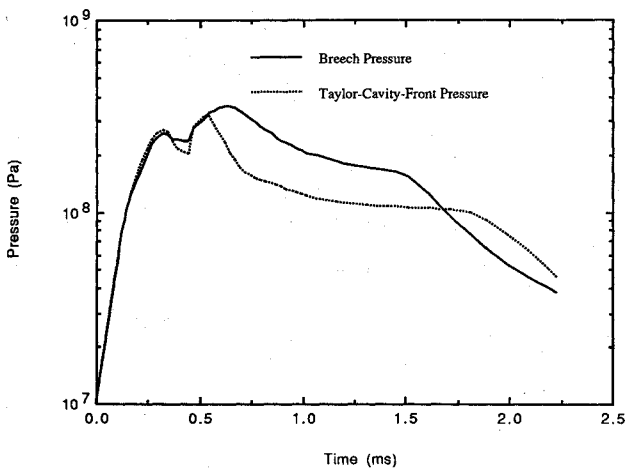

Fig. 11 Breech and Taylor cavity front pressures-time traces with a PFN discharge time of 1.6 ms and a peak power time of 1.4 ms.

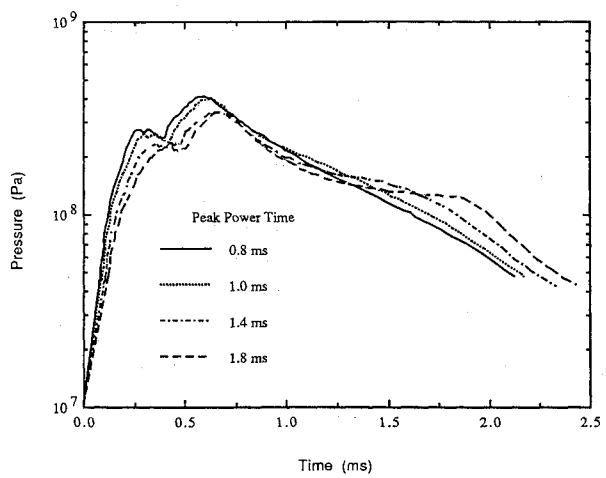

Fig. 12 Breech pressure-time traces with a PFN discharge time of 2.0 ms and various peak power times.

the case with an earlier peak power time, e.g., 339 MPa at 0.67 ms and 410 MPa at 0.60 ms for the cases with peak power time at 1.8 and 0.8 ms, respectively (see Table 2). In the second-half stage (>1.0 ms), a small hump in the pressure-time traces of the breech appears at 1.5 and 1.85 ms for the cases with peak power times of 1.4 and 1.8 ms, respectively. This discernible pressure hump is attributed to a strong plasma jet in the later stage, which results from a late peak power time. The case with the latest peak power time (1.8 ms) also has the longest constant pressure period (from 1.25 to 1.85 ms). However, the average chamber pressure during the event in this case is the lowest among the four cases, a situation not conducive to production of high muzzle velocity.

The muzzle velocities are 1936, 1924, 1882, and 1822 m/s for the cases with a peak power time of 0.8, 1.0, 1.4, and 1.8 ms, respectively, showing that the effect of chamber pressure in the early stage outweighs that in the final stage. In Table 2, the ballistic efficiencies for these four cases have a value between 10.6% and 12.0%. The case with the earliest peak power time of 0.8 ms gives the highest ballistic efficiency of 12%.

Thus, by designing the peak power time close to the end of the discharge process, lower and safter chamber pressure and longer constant pressure at the breech can be achieved, but at the expense of smaller muzzle velocity and ballistic efficiency. This design also delays the timing for transferring chemical energy to projectile kinetic energy.

Effects of the PFN Discharge Duration on Interior Ballistics

The effects of total discharge time are studied in this section. Three different PFN discharge curves with the same amount of electrical energy (0.7 MJ) and chemical energy (0.4 MJ), but with different peak power times and total discharge times, are employed. Their peak power times of 1.2, 1.4, and 1.8 ms, correspond to total discharge times of 1.4, 1.6, and 2.0 ms, respectively (see Fig. 4b). The total discharge time is 0.2 ms greater than the peak power time for all of the three cases. The condition of same amount of PFN discharge energy but different discharge times gives different peak power values, i.e., the shorter the total discharge time, the higher the peak power. Since the discharge power also controls the plasma generation rate, the shorter discharge time indicates the stronger plasma jet near peak power time.

Table 2 Results from numerical analysis for cases with various peak power times

PFN Discharge characteristics		Interior ballistic data			
Peak power time, ms	Total discharge time, ms	Event time, ms	Maximum breech pressure, Pa	Muzzle velocity, m/s	Ballistic efficiency, %
0.8	2.0	2.11	4.10[a] 10^8	1936	12.0
1.0	2.0	2.18	3.95[a] 10^8	1924	11.8
1.4	2.0	2.32	3.40[a] 10^8	1882	11.9
1.8	2.0	2.43	3.39[a] 108	1822	10.6

[a]Electrical energy 0.7 MJ; chemical energy 0.4 MJ.

Table 3 Results from numerical analysis for cases with various total discharge times

PFN Discharge characteristics		Interior ballistic data			
Peak power time, ms	Total discharge time, ms	Event time, ms	Maximum breech pressure, Pa	Muzzle velocity, m/s	Ballistic efficiency, %
1.2	1.4	2.08	4.36[a] 10^8	2048	13.3
1.4	1.6	2.22	3.55[a] 10^8	1972	12.4
1.8	2.0	2.43	3.39[a] 108	1822	10.6

[a]Electrical energy 0.7 MJ; chemical energy 0.4 MJ.

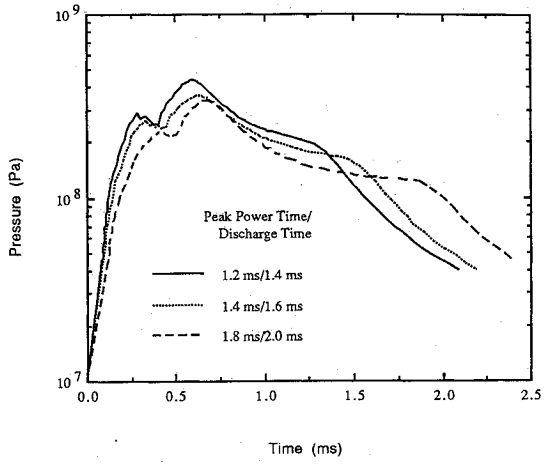

Fig. 13 Breech pressure-time traces for various PFN total discharge times and peak power times.

The pressure-time traces at the breech for these cases shown in Fig. 13 display a similar trend, with two peaks at the beginning of the event and a small hump in the later stage. The case with the shortest total discharge time (1.4 ms) gives the earliest and highest values of the first peak pressure (286 MPa at 0.29 ms). This strong initial pressurization process is a result of the vigorous plasma jet in the early stage. The maximum breech pressure, i.e., the second peak pressure, increases as the total discharge time decreases, i.e., 339, 355, and 436 MPa for the case with a total discharge time of 2.0, 1.6, and 1.4 ms, respectively (see Table 3). Note that as the total discharge time moves from 1.4 to 1.6 ms, the peak breech pressure increases by 70 MPa.

The small humps in the breech pressure-time traces in the later stage tend to coincide with the peak power time. For the case with peak power times of 1.2, 1.4, and 1.8 ms, the pressure humps occur at 1.3, 1.5, and 1.9 ms, respectively, appearing slightly later (0.1 ms) than the peak power time. It takes around 0.1 ms for the breech to respond to this maximum generating rate of plama at the PGC. After passing the small hump, the breech pressure drops quickly because the PFN discharge process is almost over and the projectile velocity is accelerating. As such, the case with shortest PFN discharge time (1.4 ms) drops the breech pressure fastest and gives the lowest value at the end of the event. The longest discharge process (2.0 ms) produces more plasma jet in the later stage; this is helpful in maintaining the breech pressure and results in the longest period of constant breech pressure. The case with the shortest total discharge time (1.4 ms) generates the strongest initial pressurization and, therefore, the highest initial projectile acceleration. Although its chamber pressure drops most quickly after 1.6 ms and has a lower acceleration, this case still gives the highest muzzle velocity of 2048 m/s.

The effects of the peak power time and total discharge time on the interior ballistic processes have been analyzed and discussed. The study shows that an earlier peak power time with the same total discharge time will increase chamber pressure, muzzle velocity, and ballistic efficiency. When the total discharge time of the PFN is extended, chamber pressure, muzzle velocity, and ballistic efficiency will decrease. The desired gun performance is to produce a high muzzle velocity and high ballistic efficiency. That can be achieved in the cases with a peak power time/total discharge time of 0.8 ms/2.0 ms (ballistic efficiency 12%), 1.2 ms/1.4 ms (ballistic efficiency 13.3%), and 1.4 ms/1.6 ms (ballistic efficiency 12.4%). Com-

Table 4 Summary of interior ballistic results from the present work and literature

(i) Measured results

Source	Gun, mm	Barrel, caliber	Projectile mass, g	Muzzle vel., km/s	Electrical eng., kJ	Working fluid	Electrical efficiency,[a] %	Max breech P, psi
Greig et al. (1988)	20	100	8	3.5	700	—[b]	7	—[b]
Greig et al. (1988)	20	100	21	2.8	700	—[b]	11.8	55,000–74,000
Greig et al. (1988)	20	100	50	2.1	700	—[b]	15.7	—[b]
Greig et al. (1988)	30	100	102	1.43	2000	—[b]	5.2	—[b]
Chrysso-mallis et al. (1988)	10	—[b]	1–6.5	1.2–1.7	190–325	Exothermic propellant	25–40	30,000–40,000
Chrysso-mallis et al. (1988)	30	85	50–380	1.1–2.75	240–850	Exothermic propellant	25–90	45,000–75,000
Chrysso-mallis et al. (1988)	90	—[b]	1100–1200	1.0–1.3	800–1100	Exothermic propellant	75–95	20,000–35,000
Chrysso-mallis et al. (1988)	105	—[b]	2000–6000	0.7–1.5	1000–4000	Exothermic propellant	90–130	20,000–40,000

(ii) Predicted results

Source	Gun, mm	Barrel, caliber	Projectile mass, g	Muzzle vel., km/s	Working fluid	Electrical eng., kJ	Total eng., kJ	Electrical efficiency, %	Ballistic efficiency,[c] %
Oberle (1988)	14	100	18	2.17	H_2O	447.8	368.6	9	10.9
Oberle (1988)	14	100	18	2.34	$LiBH_4$	449.8	406.4	10.9	12.1
Oberle (1988)	14	100	18	1.75	TiH_2/Al	77.9	222.2	35.6	12.5
Oberle (1988)	14	100	18	2.13	C_8H_{18}/H_2O_2	43.3	322.6	94.2	12.6
Present work[d]	25	100	70	1.94–2.05	C_8H_{18}/H_2O_2	700	1100	18.7–21.0	10.6–13.3

[a]Electrical efficiency = projectile kinetic energy/input electrical energy; [b]data unavailable; [c]ballistic efficiency = projectile kinetic energy/total input energy; [d]max breech pressure = 52,900–63,900 psi.

paring the peak breech pressure of these three cases, the second case has the lowest value (340 MPa). The data in Tables 2 and 3 also show that the gun performance is not optimum when the total discharge time is close to the event time. To illustrate, when the PFN total discharge time is 2.0 ms, the case with an early peak power time of 0.8 ms gives a high breech pressure of 410 MPa and the case with a late peak power time of 1.8 ms produces a low ballistic efficiency of 10.6%. Both high breech pressure and low ballistic efficiency are not desirable. From the above analysis, it can be concluded that the PFN discharge curve with a total discharge time of 1.6 ms (which is around 70% of the event time) and a peak power time of 1.4 ms (which is close to the end of discharge process) is a better design to improve the gun performance for the reactive working fluid, C_8H_{18}/H_2O_2.

Comparison of Predicted Results with Published Work

The predicted results from the present work are compared to results reported in the literature in Table 4. The predicted maximum breech pressure in the present study is between 52.9 and 63.9 kpsi (360–435 MPa), which lies in the range of the measured breech pressure, i.e., 45–75 kpsi (306–510 MPa) in the 30-mm gun developed by Chryssomallis et al.[12] The predicted maximum breech pressure also falls in the range of maximum breech pressure, 55–74 kpsi (374–503 MPa), for a 20-mm gun measured by Greig et al.[2] The predicted muzzle velocity in the present study ranges from 1.94 to 2.05 km/s, which is close to the measured muzzle velocity of 1.1–2.75 km/s in the 30-mm gun developed by Chryssomallis et al. The ballistic efficiency in the present study is 10.6–13.3%, which is better than that of 10.9–12.6% from Oberle's computer code.[1] The promoted ballistic efficiency, which indicates the higher projectile kinetic energy on the same amount of input energy, is a result of improved PFN discharge characteristics.

Conclusions

A multiphase, multidimensional, transient model has been formulated from first principles of physics to study the interior ballistic processes of an ETC gun. This theoretical model, taking into account the dynamic interactions among different phases, is capable of predicting many important performance characteristics of the gun system, such as muzzle velocity, ballistic efficiency, maximum breech pressure, projectile trajectory, and distributions of gaseous velocity and pressure inside the gun chamber. Results obtained from the present study compare well with published work.

The effects of PFN discharge time and peak power time on the interior ballistic processes have been identified in this study. By tailoring the peak power time close to the end of the discharge period, the ETC gun generates a lower value of maximum breech pressure and a longer period of constant breech pressure, but a smaller muzzle velocity and ballistic efficiency. When the PFN total discharge time is shortened, the ETC gun produces a higher muzzle velocity and ballistic efficiency at the price of a higher peak breech pressure. By designing the PFN peak power time close to the end of the PFN discharge process, and the PFN total discharge time around 70% of the event time, both muzzle velocity and breech pressure can be optimized.

Acknowledgment

The authors would like to thank George S. Chryssomallis of FMC Corp. for allowing us to use their test data for comparison with our theoretical results.

References

[1]Oberle, W. F., "A Modeling Study of Critical Factors for Optimal Electrothermal Gun Performance," BRL Technology Effort in ET Gun Propulsion, Paper 2, Vol. 1, 1988.

[2]Greig, J. R., Goldstein S. A., Tidman, D. A., and Massey, D. W., "Principles and Practice of Electrothermal Guns," the 25th JANNAF Combustion Meeting, Huntsville, AL, CPIA Publication 498, Vol. IV, Oct. 1988. pp. 245–254.

[3]Patankar, S. V., *Numberical Heat Transfer and Fluid Flow*, Hemisphere, Washington, DC, 1980, Chaps. 5 and 6.

[4]Chen, J. L., "A Theoretical and Experimental Study of the Interior Ballistic Processes of an Electrothermal Gun," PhD Thesis, Mechanical Engineering Dept., Pennsylvania State Univ., Dec. 1990.

[5]Anderson, K. E. B., "Pressure Drop in Ideal Fluidization," *Chemical Engineering Science*, Vol. 15, p. 276, 1961.

[6]Launder, B. E., and Spalding D. B., *Lectures in Mathematical Modeling of Turbulence*, Lecture 5, Academic Press, London, 1972.

[7]Soo, S. L., *Fluid Dynamics of Multiphase Systems*, Blaisdell Publishing Co., Waltham, MA, 1967, Chap. 5.

[8]Faeth, G. M., "Evaporation and Combustion of Sprays," *Progress in Energy Combustion Science*, Vol. 9, 1983, pp. 1–76.

[9]Tatterson, D. F., Dallaman, J. C., and Hanratty, T. J., "Drop Sizes in Annular Gas-Liquid Flows," *AIChE Journal*, Vol. 23, No. 1, Jan. 1977, pp. 68–74.

[10]Dallaman, J. C., Laurinat, J. E., and Hanratty, T. J., "Entrainment for Horizontal Annular Gas-Liquid Flow," *International Journal of Multiphase Flow*, Vol. 10, No. 6, 1984, pp. 677–690.

[11]Fisher, E. G., and Trippe, A. P., "Mathematical Model of Center Core Ignition in the 175 mm Gun," Calspand, Rept. VQ-5163-D-2, Picatinny Arsenal Contract DAAA 21-72-C-0577, March 1974.

[12]Chryssomallis, G. S., Marinos, C. D., Ricci, R. S., and Cook, D. C., "Combustion Augmented Plasma Gun," the 25th JANNAF Combustion Meeting, Huntsville, AL, Oct. 1988 (also through private communication).